Plasma Physics and Controlled Fusion

PAPER • OPEN ACCESS

Stability analysis of WEST L-mode discharges with improved confinement from boron powder injection

To cite this article: G Bodner *et al* 2024 *Plasma Phys. Control. Fusion* **66** 045022

OPEN ACCESS
IOP Publishing

Plasma Physics and Controlled Fusion

Plasma Phys. Control. Fusion 66 (2024) 045022 (15pp)

https://doi.org/10.1088/1361-6587/ad2c29

Stability analysis of WEST L-mode discharges with improved confinement from boron powder injection

G Bodner[1,*], C Bourdelle[2], P Manas[2], A Gallo[2], K Afonin[2], A Diallo[1], R Lunsford[1], Ph Moreau[2], A Nagy[1], F Clairet[2], C Gil[2], E Tsitrone[2], L Vermare[3] and the WEST Team[4]

[1] Princeton Plasma Physics Laboratory, Princeton, NJ, United States of America
[2] CEA, IRFM, F-13108 Saint-Paul-Lez-Durance, France
[3] École Polytechnique—LPP, Paris, France

E-mail: bodnerg@fusion.gat.com

Received 9 May 2023, revised 17 January 2024
Accepted for publication 22 February 2024
Published 12 March 2024

Abstract

WEST L-mode plasmas with dominant electron heating and no core torque source have observed improvements in confinement during boron (B) powder injection. These results are reminiscent of previous powder injection experiments on other devices and gaseous impurity seeding experiments on WEST. During powder injection, the stored energy increased up to 25% due to enhanced ion and electron heat and particle confinement. The improvements in confinement were not indicative of an L-H transition. To identify the dominant mechanisms and the causality chain behind these improvements in confinement, we employ interpretative modeling using METIS, predictive integrated modeling using a high-fidelity plasma simulator (HFPS), and stand-alone gyrokinetic simulations using quasi-linear gyrokinetic code. Interpretative modeling with METIS allowed for the estimation of missing data while maintaining good overall consistency with experiment. These results provided the initial conditions for fully predictive flux driven simulations using the HFPS. From these simulations, quasi-linear gyrokinetic analysis was performed at $\rho = 0.5$ and $\rho = 0.65$. Collisionality was found to be a strong candidate for the turbulence suppression mechanism at $\rho = 0.5$, while a combination of collisionality and the T_e/T_i ratio was found to be the likely mechanism at $\rho = 0.65$. The results additionally suggested that increased Z_eff (through main ion dilution) could play a role in the improved confinement, but this could not be confirmed due to a lack of experimental measurements. The modeling framework established here can now be used to evaluate and exploit a variety of future powder injection experiments.

Keywords: transport, powder injection, impurity injection, confinement, QuaLiKiz

1. Introduction

ITER, SPARC, and future fusion pilot plants will need to exhaust large amounts of energy in order to protect the plasma facing components (PFCs) from melting and/or cracking [1, 2]. This problem is compounded by plasma-material interactions as the high energy plasma exhaust can sputter the first wall/divertor material into the core plasma. Tungsten (W) is the chosen material for the ITER divertor [1] and the SPARC PFCs [3] and has been shown to severely degrade plasma performance (i.e. reduced W_th and T_e) if sputtered into the core plasma as the W will radiate the much-needed stored energy out of the plasma [4]. To prevent this, ITER and future pilot

[4] http://west.cea.fr/WESTteam.
[*] Author to whom any correspondence should be addressed.

plants will likely operate in a detached divertor regime [5], where the plasma will be separated from the divertor PFCs by a low temperature ($T_e < 5$ eV), radiative region. Plasma detachment is typically achieved using impurity injection (powder dropping, gas puffing, pre-shot glow discharge deposition) which spreads the exhausted energy over the entire vessel area through line radiation. This operational regime reduces the heat fluxes to the PFCs and reduces the W sputter yield which is a function of the PFC target temperature.

In addition to power exhaust, impurity injection has been extensively investigated as a mechanism to improve plasma performance. The controlled injection of impurities into high temperature plasmas has often been linked to increased temperatures and/or densities through the suppression of turbulence by various mechanisms [6, 7]. Impurity injection has the potential to combine a low T_e radiative boundary (necessary to protect the PFCs) with improved core performance (necessary to increase the fusion yield); a highly desirable scenario for a fusion pilot plant. One of the most notable demonstrations of this scenario was the radiative improved (RI) mode developed on TEXTOR. These discharges were achieved using impurity seeding from feedback-controlled neon/argon injection or sputtering from a siliconized wall [8]. TEXTOR RI-modes were characterized by H-mode-like confinement, a large radiative fraction, high density, and the absence of edge-localized modes (ELMs). While these parameters make for an attractive operating scenario, reproduction of these results on medium to large size machines, such as DIII-D and JET, has proven to be challenging [8].

Recently, experiments on WEST using boron (B) powder injection have observed results reminiscent of RI-modes (elevated core density and improved confinement). These results encourage the possible use of powder injection on ITER and a future pilot plant. Particulate/powder injection first gained popularity for its potential as an active wall conditioning mechanism. Powder injection uses the high temperature plasma to ablate and then deposit the injected material onto the PFCs. This allows for wall conditioning in the presence of the magnetic field (i.e. active conditioning); necessary for long-pulse operation where glow-discharge boronization is not feasible. The use of inert powders (such as boron or boron-nitride) is additionally safer than traditional boronated gases (such as diborane) which are explosive and toxic. To evaluate powder injection as an active conditioning technique, impurity powder droppers (IPDs) [9] have been installed and operated on several tokamaks and stellarators worldwide [10–17].

WEST provided a unique test bed for the IPD as an active conditioning technique and power exhaust mechanism due to its reactor-relevant capabilities as a superconducting tokamak with a full-W environment [18–20]. On WEST, B powder injection experiments in lower single null L-mode plasmas observed both improved wall conditions and improved plasma performance. This paper evaluates these improvements in confinement using interpretative and integrated modeling to identify and isolate possible turbulence suppression mechanisms that can be exploited in future experiments.

A summary of the B powder injection experiments on WEST is given in section 2. Section 3 provides an overview of the modeling framework and describes the codes used to simulate WEST discharges. Section 4 details the gyrokinetic analysis and the impact of B powder on the electron and ion particle and heat fluxes. Lastly, section 5 concludes with a discussion of the modeling results and how they may be applied to future experiments.

2. Boron powder injection experiments on WEST

2.1. Experiment overview

This section will provide a brief overview of the B powder injection experiments from the WEST C5 campaign with a focus on the improvements in plasma confinement. A full summary of the C5 experiments and their impact on wall conditioning can be found in [17]. To investigate the viability of B powder injection in a full-W environment and on long-pulse time scales, an IPD was commissioned on WEST in early 2021. After installation and commissioning, B powder was dropped into 10 lower single null (LSN) L-mode deuterium (D) plasmas. These discharges featured plasma current $I_\mathrm{p} = 0.5$ MA, toroidal field $B_\mathrm{T} = 3.7$ T, lower hybrid current drive (LHCD) power $P_\mathrm{LHCD} \sim 4.5$ MW, edge safety factor $q_{95} = 4.3$, and volume- averaged electron density $n_e \sim 3.5 \times 10^{19}$ m^{-3} (Greenwald density fraction $n_\mathrm{g} = 0.45$). Ohmic and LHCD were the only methods of heating/current drive used in these experiments (LHCD turns on at $t = 5$ s). Various powder drop rates were tested to determine the optimal drop rate for future experiments. The WEST diagnostic suite for these experiments was comprised of interferometry (core n_e), reflectometry (edge n_e), doppler reflectometry (ExB profile), electron cyclotron emission (core T_e), fission chambers (neutron rate), visible and ultraviolet spectroscopy (impurity line radiation), embedded Langmuir probes (SOL T_e and n_e), bolometry (P_rad), and magnetics (I_p, W_MHD, etc).

Figure 1 shows several key parameter traces for WEST discharges with and without powder injection. During the B drop, improvements in the stored energy, DD neutron rate, electron temperature, and core density peaking (shown in figure 3) were observed. Here, the DD neutron rate is taken as a proxy for the ion temperature. These improvements occurred despite minimal changes to the plasma current and LHCD power and an increase in the radiated power, implying improved confinement. Similar increases in confinement have been observed on several other tokamaks/stellarators using boron, boron-nitride (BN), and lithium powder injection [10, 12, 15, 17, 21–27].

The improvements in confinement seemed to impact the electrons and ion channels differently. Shot 56 919, which had a modest drop rate of 9.2 mg s^{-1}, showed that the DD neutron rate was almost agnostic to the electron density. Concurrent with the powder drop, the neutron rate increased and stayed at an elevated level, despite the electron density rising and then falling. The electron temperature, alternatively, appeared to be linked to the density. During the initial density increase, the electron temperature decreased and then rebounded as the B powder began to fully assimilate. In the case where the discharge survived the powder assimilation

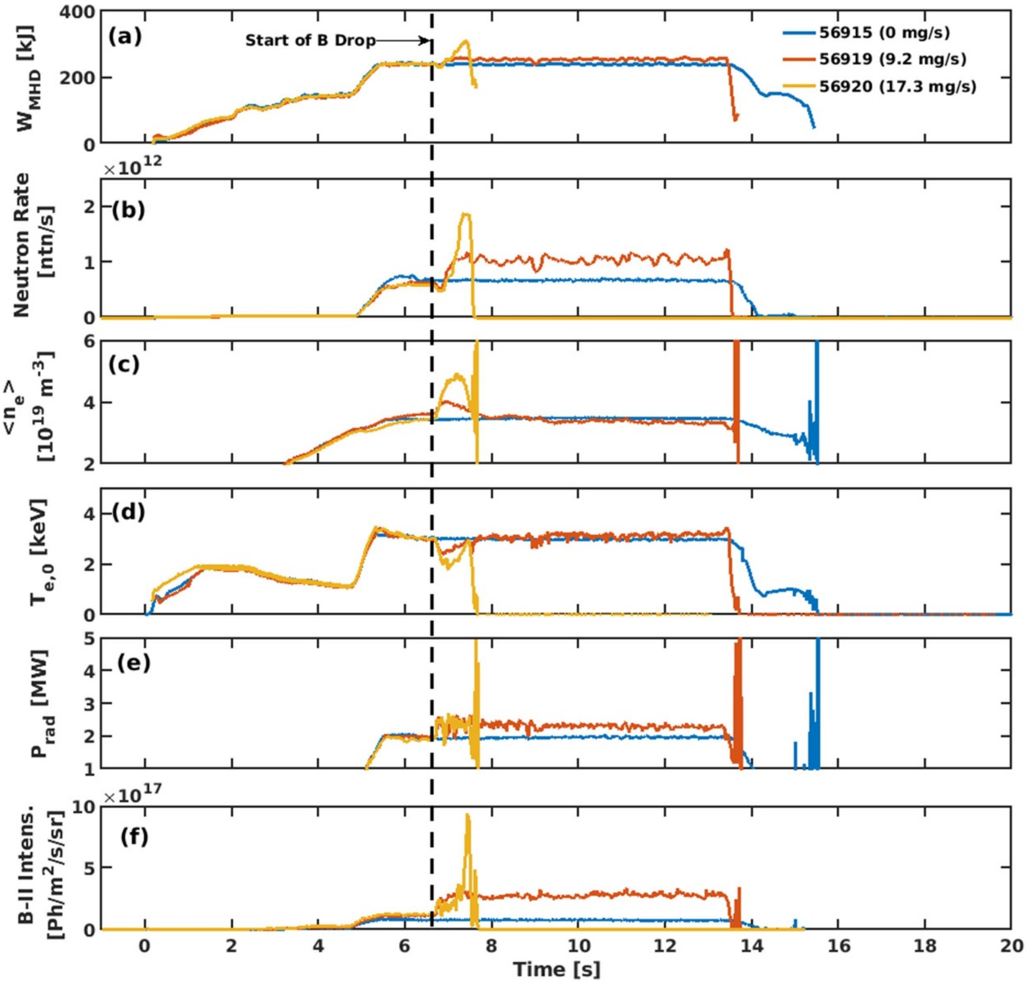

Figure 1. (a) W_{MHD}, (b) DD neutron rate, (c) $\langle n_e \rangle$, (d) $T_{e,0}$, (e) $P_{rad,tot}$, and (f) B-II line intensity at the lower outer divertor for two WEST discharges with powder injection (56 919 and 56 920) and one without (56 915).

(56 919), the electron temperature increased above that of the case without B injection [17]. Understanding the mechanisms behind these differences may provide insights into the improved confinement.

This paper focuses on shot 56 920 (yellow traces in figure 1) which featured the largest improvements in confinement with a 25% increase in the stored energy and a 200% increase in the neutron rate. While this discharge disrupted after 400 ms of powder injection, the improved confinement was not believed to be a transient effect. At more modest drop rates, such as in shot 56 919 (orange traces), the improved confinement lasted the entire drop duration. The disruption was likely due to a larger than expected drop of boron powder which then triggered a radiative collapse. For 56 920, there was an anomalously large attenuation of the flowmeter signal (which measures the powder drop rate) around the disruption time, indicating that a large quantity of boron powder was dropped into the plasma. This may have been the result of powder build-up near the drop tube entrance or the high input voltage which may increase the fluctuations in drop rate. Operating at higher auxiliary heating power should enable the sustainment of higher drop rates and prevent disruptions from off-normal drops. This hypothesis will be tested in future experiments.

2.2. Possible mechanisms for improved confinement

Further analysis of these discharges suggested the change in confinement was not indicative of an L-H transition. L-H transitions in WEST observed the formation of a density pedestal, a substantial reduction in the plasma internal inductance ℓ_i (due to the increased bootstrap current), and the formation of a radial electric field E_r well [18, 20]. By contrast, in the powder injection experiments, the density increases were observed primarily in the core and were not accompanied by reductions of ℓ_i or formations of E_r wells. The change in the $E \times B$ velocity profile due to powder injection, measured by Doppler reflectometry and proportional to E_r, is shown in figure 2. The center of the well seemed to be pushed radially outward, however the magnitude stayed relatively the same. This is in contrast to L-H transitions in WEST, where the magnitude of the $E \times B$ velocity well decreased by $\sim$ 3 km s^{-1} from -2 km s^{-1} to -5 km s^{-1} after the L-H transition [28]. Lastly, no signatures of ELMs were present in the fast camera video or D_γ signal.

As mentioned previously, the RI-mode was one of the most attractive scenarios developed using impurity injection. In those discharges, core density peaking was the predominant

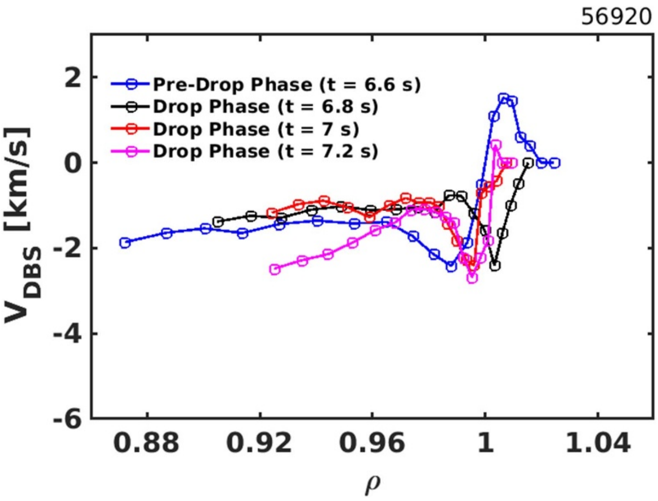

Figure 2. $E \times B$ velocity profile from doppler reflectometry at one time point before and several time points during the B drop. B powder was dropped at $t = 6.7$ s.

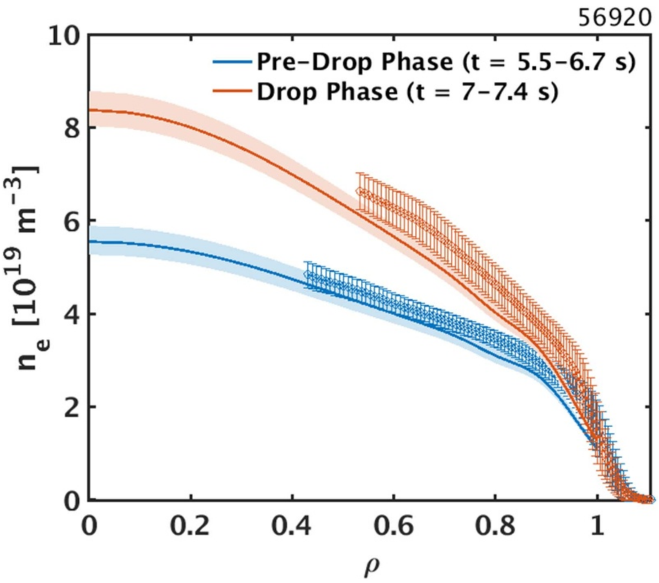

Figure 3. Density profiles from time-averaged interferometry inversions (solid lines) and reflectometry measurements (markers with error bars). Colors denote the time-average windows used: pre-drop phase (blue) and drop-phase (red).

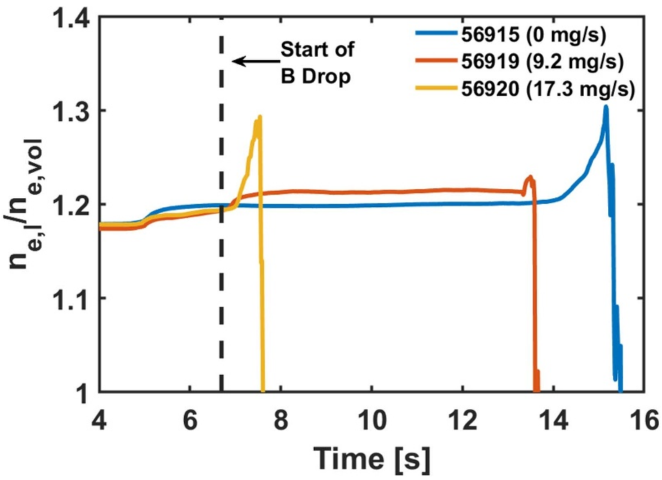

Figure 4. Ratio of the line-averaged core density ($\rho = 0.02$) with the volume-averaged density for three discharges with different powder drop rates.

mechanism responsible for the suppression of ion-temperature gradient (ITG) driven turbulence [8]. Similar to the RI-modes on TEXTOR, core density peaking was observed during the B powder injection experiments in WEST. Figure 3 shows an increase in the core electron density during the powder drop phase compared to the pre-drop phase. These profiles correspond to time-averages from fitted interferometry inversions (solid lines) and reflectometry measurements (markers with error bars). Even though the powder injection site is localized to the edge, there was significant density peaking from $\rho \leqslant 0.8$. This increase in core density was not attributed directly to the ionization of the B powder as simulations from SOLEDGE-EIRENE and DIS of WEST discharges with B powder injection indicated that the B atoms become fully ionized at $\rho > 0.9$ [29]. Therefore, the peaking of the core density was likely due to modified particle transport rather than a modified particle source.

The peakedness of these profiles was evaluated by taking the ratio of the line-averaged density from a central-viewing interferometry chord ($\rho = 0.02$) with the volume-averaged density. Flat density profiles will give ratios ~ 1, while peaked profiles will give ratios > 1. The density peaking ratios for the discharges presented in figure 1 are shown in figure 4. There is a noticeable non-linear increase in the density peaking after powder injection begins and the traces strongly resemble the stored energy and neutron rate traces from figures 1(a) and (b). Furthermore, the density peaking seemed to increase with the powder drop rate, possibly due to increased Z_{eff}.

Indeed, the importance of Z_{eff} on core density peaking was highlighted when other medium to large size machines, such as DIII-D and JET, attempted to reproduce the RI-mode but were unable to obtain the density profile bifurcation observed in TEXTOR. The prevailing theory is that a critical Z_{eff} is needed to obtain this profile bifurcation, and this critical Z_{eff} differs depending upon various machine characteristics [8]. If so, future powder injection experiments may benefit from increased powder drop rates to obtain the critical Z_{eff}. Predictive capabilities on this front are therefore highly desired as large increases in Z_{eff} will result in unacceptable levels of fuel dilution.

In addition to the core density, there were also modifications to the edge density. A small inward shift in the edge density gradient was observed around the separatrix, likely due to a reduction in wall fueling from the B powder [17]. Further analysis showed no large variations in the separatrix density; however, it is difficult to make any gradient-based conclusions on turbulence suppression due to the spread ($\sim$10%) in the reflectometry data.

Lastly, fuel dilution may have played a significant role in the turbulence suppression. This was the case for gaseous N_2 seeding experiments on WEST, which observed increases in confinement without density profile modification [30]. Unfortunately, uncertainties in the visible bremsstrahlung signal prevented measurements of Z_{eff} during the WEST powder injection experiments. Resistive estimates of Z_{eff} ($\sim$1.73), calculated during the Ohmic phase of the discharge (0–5 s), showed no large changes following a discharge with B powder injection. The use of LHCD powder prevents resistive estimations of Z_{eff} during the B drop.

Experimental trends presented in [17] showed some correlation of stored energy with the level of D recycling. The further the D recycling was suppressed the larger the increases in stored energy, possibly due to further fuel dilution resulting from less wall fueling. To confirm the dominant turbulence suppression mechanism(s), interpretative modeling using METIS [31], predictive modeling using a high-fidelity pulse simulator (HFPS) [32], and a quasi-linear gyrokinetic code (QuaLiKiz) [33] were employed.

3. Modeling framework for the WEST powder injection discharges

Shot 56 920 was chosen as the modeling fiducial due to its large improvements in confinement when compared to the other powder injection discharges. The significant changes in stored energy and neutron rate from this discharge likely meant more noticeable changes in the particle and/or heat fluxes than in those discharges with more modest drop rates and improvements in confinement. Therefore, analysis was concentrated on this discharge despite its short pulse duration. Future powder injection discharges will aim to have similar or higher improvements in confinement with longer pulse and drop durations. These discharges will provide more rigorous testing for the framework developed in this paper.

The modeling framework is as follows: METIS was used to supplement experimental measurements by estimating missing quantities through an integrated modeling approach. This combination of experimental and estimated measurements from METIS was then used as the initial condition for fully predictive simulations using the HFPS, which evolved the density/temperature profiles over time. The resultant profiles from the HFPS simulations were then used in the gyrokinetic stability analysis. A diagram of this workflow is shown in figure 5.

3.1. Preparation of dataset using interpretative modeling with METIS

While the WEST diagnostic suite was able to survey a number of key plasma parameters, several inputs necessary for gyrokinetic analysis were not measured. For example, the ion temperature profile and its resulting gradient lengths were unavailable for this campaign (these measurements will be available for future experiments using a recently installed x-ray crystal spectrometer). In addition, the experimental measurement of the current profile (typically done through the motional stark effect) was not available due to the absence of diagnostic neutral beams on WEST. Lastly, ECE measurements of the electron temperature profile were constrained to $\rho < 0.5$ due to light pollution from LHCD. Without these experimental measurements, transport modeling was limited in accuracy due to degrees of freedom in important input parameters such as the ion temperature gradient. Therefore, interpretative modeling with METIS was used to constrain the missing experimental measurements needed for the initial and boundary conditions of the predictive integrated modeling. These predicted profiles could then be used as input for the stand-alone gyrokinetic modeling. Here, stand-alone refers to the use of the code outside of a self-consistent or predictive loop.

METIS is a fast 1.5D tokamak modeling code that allows for the interpretative/predictive modeling of discharges from a variety of tokamaks (e.g. AUG, JET, and WEST). The code balances speed and performance by combining 0D confinement scalings with 1D current diffusion models and 2D plasma equilibria to build a self-consistent picture of the transport processes in the plasma. METIS has been used in past interpretative analysis of WEST L-mode discharges with gaseous nitrogen injection [30]. An extensive background on the foundation and workflow of METIS is given in [31]. Therefore, only a summary on the relevant portions of the code will be highlighted here.

For inputs, METIS (in interpretative mode) takes in a variety of experimental plasma parameters such as the plasma geometry, plasma equilibria, radiated power, stored energy, and any available kinetic profiles. The thermal energy content and plasma geometry were taken from 2D NICE equilibrium reconstructions constrained by magnetics and polarimetry [34]. The fitted electron temperature and density profiles were taken from ECE and interferometry, respectively.

Various assumptions were then made to constrain the missing experimental measurements while ensuring global data consistency. For the ion temperature, the profile shape was assumed to have the form $T_{\text{i}} \propto \sqrt{n_e T_e}$ with the magnitude for T_{i} on axis fitted to be self-consistent with the measured DD neutron rate. Due to light pollution in the visible bremsstrahlung wavelength range, Z_{eff} was estimated to match the measured flux consumption during the Ohmic phase of the discharge (0–5 s). This resulted in a flat Z_{eff} profile estimate of 1.73. The treatment of light impurities was additionally simplified by assuming only nitrogen was present. Lastly, tungsten was chosen as a representative high-Z impurity, and its concentration was scaled to match the experimentally observed radiated power from bolometry. Due to the large cooling coefficient of W, its impact is predominantly observed in the radiated power and not in the Z_{eff}, as a plasma could not tolerate a substantial concentration of W. The available experimental data and assumptions that went into the model are summarized in table 1.

Using these assumptions, an interpretative METIS simulation was conducted on shot 56 920. The consistency between experimental and simulation is shown in figure 6, where the estimated stored energy content from METIS (derived from the estimation of missing quantities) had less than a 7% difference than the stored energy calculated by NICE (constrained by magnetics and polarimetry angles) during the LHCD phase and even better agreement during the powder drop.

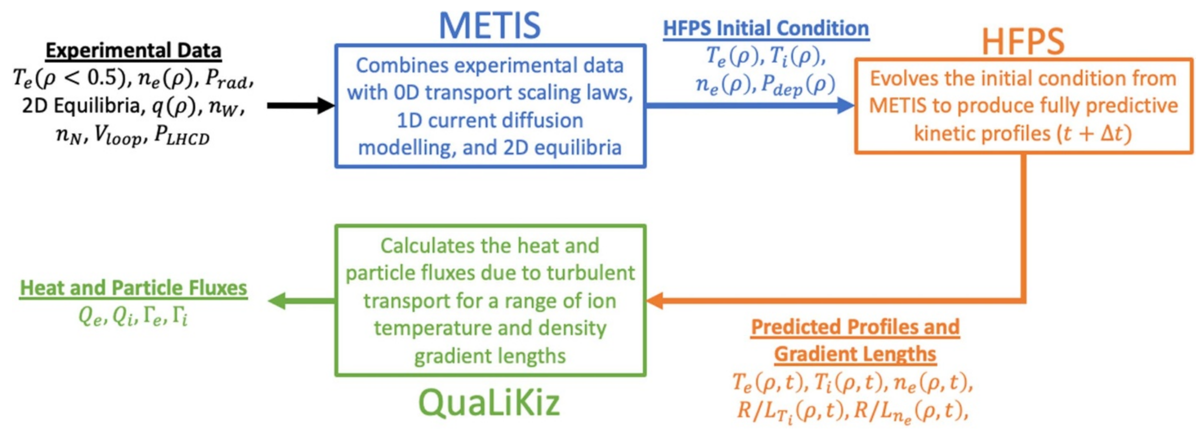

Figure 5. Modeling workflow showing the interplay between METIS, the HFPS, and QuaLiKiz.

Table 1. List of key diagnostics used in the C5 B powder experiments and a list of the assumptions used in the METIS modeling to estimate the missing measurements.

Experimental Data	Desired Quantity
Electron cyclotron emission	$T_e(\rho < 0.5)$
Interferometry	$n_e(\rho)$
Reflectometry	$n_{e,\mathrm{edge}}(\rho)$
Magnetics/Polarimetry	2D equilibria, q, W_{MHD}
Fission chambers	DD neutron rate
Bolometry	P_{rad}
Assumptions	**Desired Quantity**
Z_{eff} is equal to the measured flux consumption during the Ohmic phase and flat across the profile	Z_{eff}
T_{i} scales with neutron rate and the profile has the shape of $\sqrt{T_e/n_e}$	$T_i(\rho)$
Low-Z impurities dominate, assume mostly N with W content scaled to match P_{rad}	n_{W}
LHCD power deposition model [31]	$P_{\mathrm{dep}}(\rho)$, Core source profile for electrons

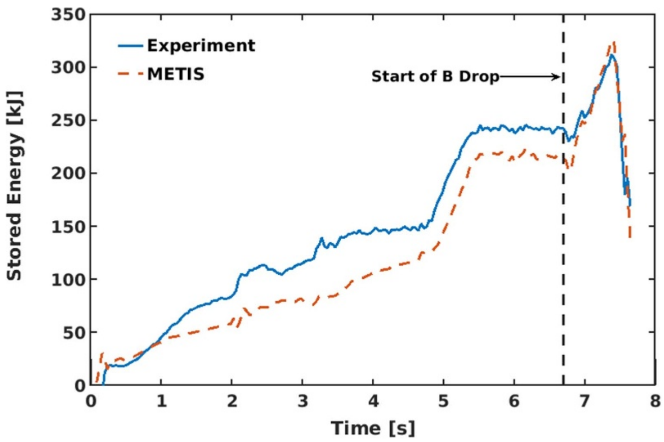

Figure 6. Comparison of stored energy calculated by NICE and constrained by magnetics/polarimetry angles (solid blue line) with the simulated result from METIS (dashed orange line).

3.2. Kinetic profile predictions from the high-fidelity plasma simulator

A HFPS was then used to evolve the initial conditions provided by the combined set of tools and assumptions described in table 1, over the entire LHCD heating phase. Two important points were addressed with these predictive simulations. First, the capability of the models used in reproducing the increase in plasma energy confinement was assessed. Second, the simulations provided a good starting point for stand-alone gyrokinetic analysis (performed with the same transport code, QuaLiKiz) since the output profiles were constrained by the flux driven approach taken in the integrated modeling.

The HFPS uses the IMAS (ITER Integrated Modeling & Analysis Suite) format data as input and output. It is based on the JINTRAC suite of codes [35] (with JETTO as the transport module) which have been widely used and whose predictive capabilities have been validated against JET experiments [32, 36]. JETTO is a 1.5D transport code that solves the plasma transport equations averaged over magnetic flux surfaces characterized by the Grad–Shafranov equation. These equations characterize the electron and ion temperatures, the main ion density, and the current diffusion.

For the transport models, QuaLiKiz was used for the turbulent transport (without toroidal rotation physics) and NCLASS for the neoclassical transport (here the tungsten density was not evolved). A residual background of Bohm-like transport was additionally used to ensure numerical stability. The LHCD heating source was not self-consistently modeled but was prescribed at each time as described in table 1. Finally, the boundary conditions were set to $\rho = 0.8$ (normalized toroidal magnetic flux). The settings of the predictive HFPS simulation are summarized in figure 7. The quantities in red are self-consistently predicted, while the quantities in blue are taken via the data preparation from table 1.

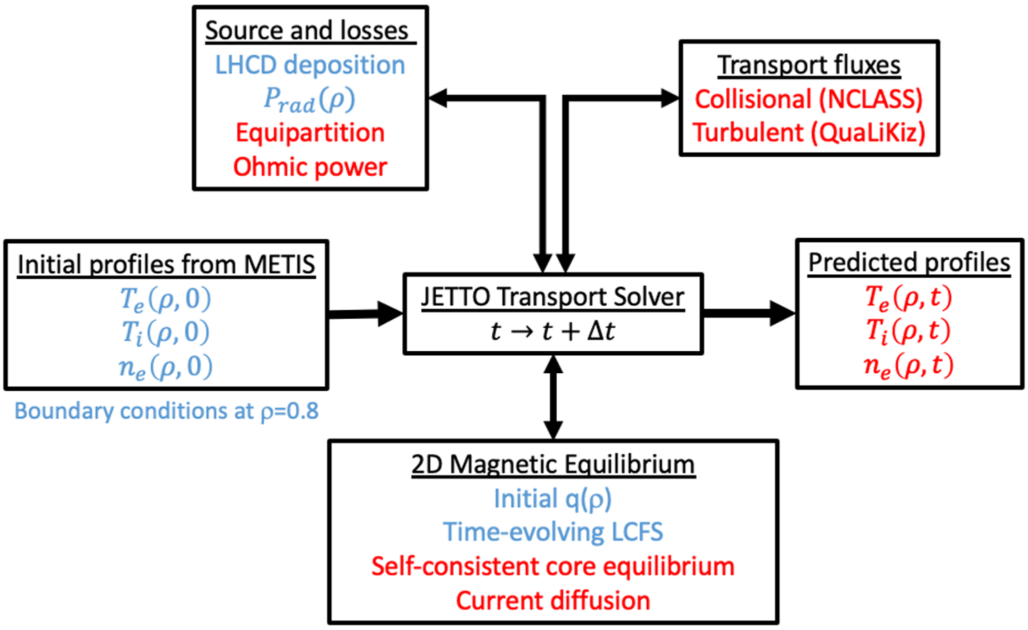

Figure 7. HFPS workflow showing the generation of the fully predicted electron and ion temperature/density profiles. The quantities in red are self-consistently predicted, while the quantities in blue are taken via the data preparation from table 1.

Figure 8 shows that the predicted time traces from the HFPS were able to accurately capture the large density increase ($t = 7$–7.4 s) from the powder assimilation as well as the associated reduction in temperature. We note that there was some discrepancy in the central electron temperature after $t = 7$ s (blue traces in figure 8(b)). This is likely due to the sensitivity of T_e in the central region ($\rho < 0.3$) to the heating and radiated power since turbulent transport is reduced. Nevertheless, the discrepancy in T_e was less pronounced at mid-radius where the gyrokinetic analysis was performed (orange traces in figure 8(b)). Figure 8(c) shows a comparison of predicted stored energy from the HFPS ($\mathrm{W_{th}}$, predictive) against the magnetic reconstruction ($\mathrm{W_{MHD}}$, NICE) and the interpretative thermal energy content based on the measured and inferred profiles as described in table 1 ($\mathrm{W_{th}}$, interpretative). The predicted values were within 30% of the experimental values and capture the qualitative trends, in particular the increment in energy content at the time of the boron drop. There was a slight drop in stored energy in the HFPS case at the LHCD turn-on time ($t = 5$ s) which was likely due to a discrepancy between the computed LHCD deposition profile and the experimental profile at that time. This discrepancy, however, was short lived and the experimental trend was recovered quickly. The agreement between experiment and the HFPS simulations provided confidence for its use as input to the gyrokinetic code.

From the predicted profiles, normalized gradient lengths of the electron temperature and density, defined as: $R/L_{T_\mathrm{i}} = -R\nabla T_\mathrm{i}/T_\mathrm{i}$ and $R/L_n = -R\nabla n/n$, were then calculated as a function of both normalized radius and time. These particular gradient lengths were chosen to isolate the impact of core density peaking on the ion temperature profile. Normalized gradient lengths for the ion temperature and electron density at mid-radius ($\rho = 0.5$) are shown in figure 9(b) for various times during the discharge. The volume-averaged density from 56 920 is provided in figure 9(a) to show the time points of the gradient lengths with respect to the powder drop. As the powder assimilated into the plasma, the ion temperature and electron density gradient lengths both increased, which is consistent with the observed increases in the electron density and neutron rate (αT_i).

In addition to the normalized gradient lengths, the HFPS simulations calculated relevant flux driven transport quantities such as the turbulent electron particle and heat flux (Γ_e, Q_e), and ion heat flux (Q_i) profiles. Figure 10 shows these quantities as function of time for the radial locations of $\rho = 0.5$ and $\rho = 0.65$. Note that the particle flux was not strictly zero since these are not steady state solutions (i.e. the time derivates of n_i, T_i, and T_e are not zero) and due to contributions from the Ware pinch. The electron heat source was dominated by LHCD heat deposition and the ion heat source by equipartition in theses electron heated plasmas. The resultant traces were used to determine the contours of particle and heat flux detailed in the gyrokinetic analysis presented in the next section. Gyrokinetic simulations were first performed at $\rho = 0.5$ due to stronger confidence in the data quality. Simulations done at $\rho > 0.5$ were more reliant on profile fitting due to missing ECE measurements and simulations at $\rho < 0.5$ had difficulties converging to sensible values. Therefore, the domain investigated was limited to $\rho = 0.5$ and $\rho = 0.65$. Additionally, these radial locations were sufficiently inboard to ensure full ionization of the B powder ($T_e \geq 2$ keV [17]). Future experiments with more extensive diagnostic coverage should be able to expand the radial domain of this modeling workflow.

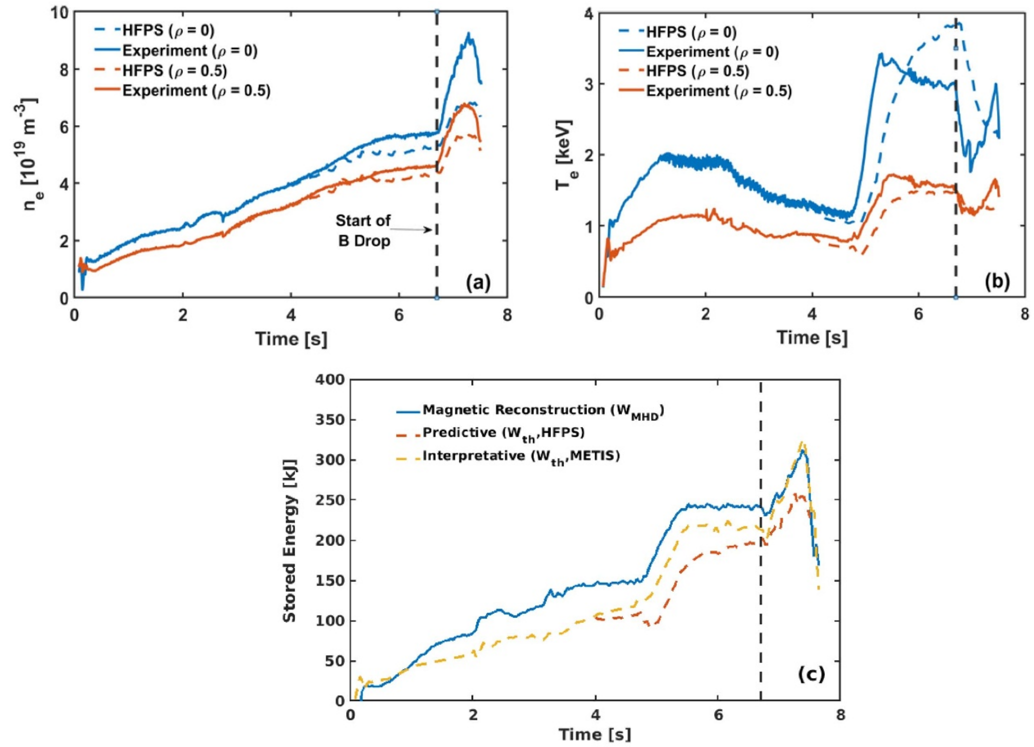

Figure 8. Comparison of electron density (a) and electron temperature (b) traces at $\rho = 0$ and $\rho = 0.5$ from the HFPS and experimental measurements. (c) Comparison of W_{MHD} from the magnetic reconstruction, W_{th} from METIS in interpretative mode, and predicted W_{th} from the HFPS.

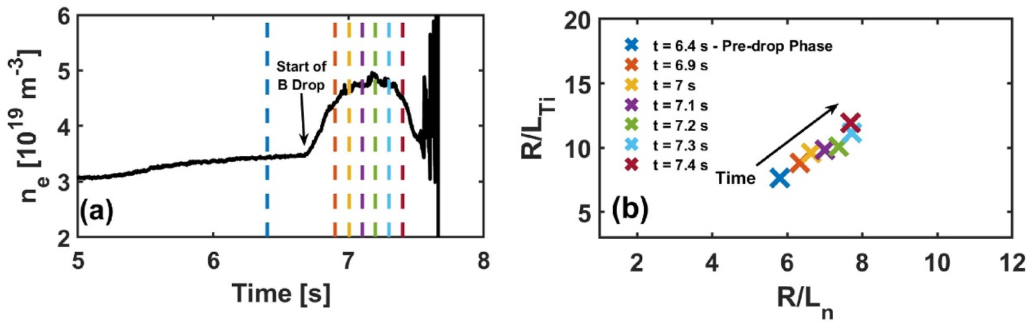

Figure 9. (a) Volume-averaged n_e from interferometry showing the various simulation times throughout the B drop. (b) R/L_{T_i} and R/L_n values from the HFPS at $\rho = 0.5$ for the different simulation time points.

3.3. Stand-alone gyrokinetic simulations with QuaLiKiz

To explore the key mechanisms leading to the improved confinement, we tested the impact of various parameters individually using a turbulent transport code. Two choices needed to be made concerning the input parameters of the reference case and concerning the turbulent transport code. For the inputs of the reference case, we used the HFPS predicted profiles at 6.4 s (prior to the B drop) as a set of self-consistent data. The current profile was consistent with the plasma resistivity and the energy content was obtained based on the predicted temperature and density profiles was consistent with the equilibrium reconstruction from NICE (figure 8(c)). For the turbulent transport code, we used QuaLiKiz, a gyrokinetic quasilinear turbulent transport code. In this implementation, the collisionality operator of QuaLiKiz has been improved and in particular the handling of trapped electron modes (TEMs) was more accurate when compared to higher hierarchy models such as the gyrokinetic code GENE [37]. QuaLiKiz is about 2 orders of magnitude faster than linear simulations with GENE or GKW. This is due to the fact that the eigenfunctions are not resolved self-consistently, unlike in GENE and GKW, but are approximated in the fluid limit. This approximation has been extensively demonstrated in [33, 37] and the references therein.

In this stage of the workflow, QuaLiKiz was used in a stand-alone capacity, meaning that the outputs were not influenced by any self-consistent loops. To evaluate the impact of various

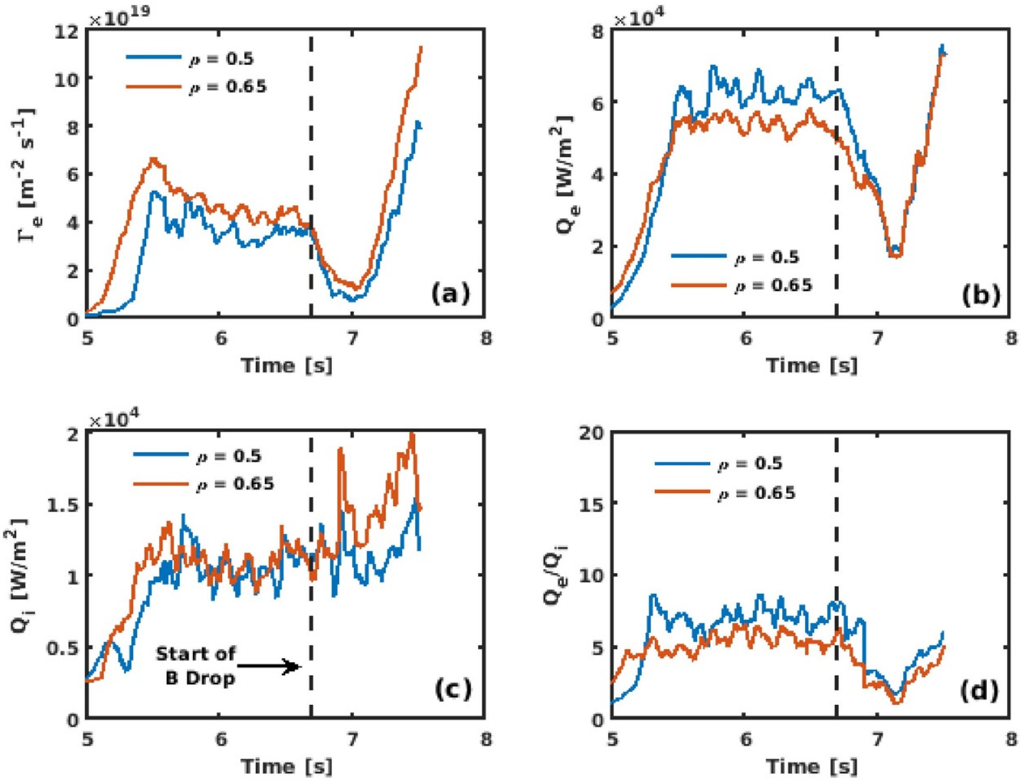

Figure 10. (a) Γ_e, (b) Q_e, (c) Q_i, and (d) Q_e/Q_i traces from the HFPS simulations at $\rho = 0.5$ and $\rho = 0.65$.

parameters on the turbulent fluxes, a 2D scan of the plasma stability was performed over a range of normalized gradients of R/L_{T_i} and R/L_n. This provided a broad domain over which to observe any changes to the heat and particle flux contours. The analysis presented in the next section is therefore more qualitative than quantitative, as the missing experimental measurements preclude any consistent error analysis. Nevertheless, these simulations should provide insights into the simultaneous increased density peaking and increased ion temperature, shown in figure 9(b), from the B drop.

To perform this scan, a 2D grid with the ion temperature gradient length (R/L_{T_i}) on one axis and the electron density gradient length (R/L_n) on the other was created. Using this grid, the electron particle flux, electron heat flux, and ion heat flux were calculated over a range of gradient lengths, normalized radii, and time. Relevant plasma parameters (such as ν_e^*, q, s, …) were taken from the HFPS simulations to constrain the gyrokinetic modeling.

The results of a representative QuaLiKiz simulation are shown in figure 11. This simulation corresponds to particle flux and electron-ion heat flux contours calculated for $t = 6.4$ s (before the B drop). The background color map represents a wide range of electron particle flux contours from 0 to 6 × 10^{20} $\mathrm{m}^{-2}\,\mathrm{s}^{-1}$, the white line represents the electron particle flux contour from the HFPS, and the black line represents the electron-ion heat flux ratio (Q_e/Q_i) at mid radius (4.8 in this dominantly electron heated pulse). The blue box highlights the crossing of the two flux contours. In the following section, several quantities are varied from the nominal inputs to evaluate the changes in the intersections and thus the predicted changes in R/L_{T_i} and R/L_n.

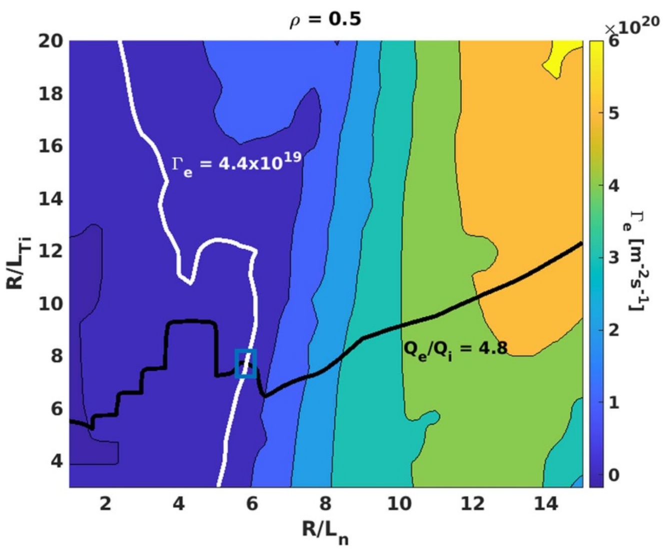

Figure 11. Contours of electron particle flux from QuaLiKiz at $t = 6.4$ s and $\rho = 0.5$. The white line corresponds to the particle flux contour at 4.4×10^{19} $\mathrm{m}^{-2}\mathrm{s}^{-1}$ and the black line corresponds to the electron-ion heat flux ratio contour at 4.8.

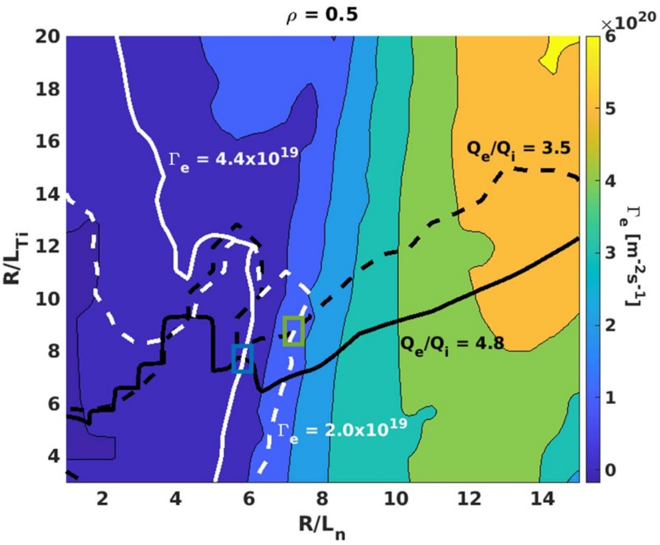

Figure 12. Contours of electron particle flux and electron/ion heat flux ratio from QuaLiKiz at $\rho = 0.5$ for $t = 6.4$ s and $t = 7.2$ s. The solid lines correspond to simulations at $t = 6.4$ s (before the B drop) and the dashed lines correspond to simulations at $t = 7.2$ s (during the B drop). The colored contours in the background only correspond to the simulation at $t = 6.4$ s.

4. Exploring the impact of key parameters on turbulent heat and particle transport with QuaLiKiz

4.1. Effect of boron powder on gradient contours

With the modeling framework established, QuaLiKiz simulations were then run on a range of time points from shot 56 920. Figure 11 showed a QuaLiKiz simulation for just a single time point ($t = 6.4$ s) before the B drop. Using the HFPS simulations as inputs, similar contour plots were generated for several time points during the B drop as well. A comparison of QuaLiKiz contours from before ($t = 6.4$ s, solid lines) and after ($t = 7.2$ s, dashed lines) the B drop is shown in figure 12. This time point was chosen since it was at the peak of the density rise. The change in the contour crossing (blue and green boxes) illustrates the impact of the B powder on the predicted R/L_{T_i} and R/L_n satisfying both conditions on the particle flux and heat flux ratio. Powder injection pushes both the electron particle flux contour to higher R/L_n and pushes electron/ion heat flux ratio to higher R/L_{T_i} resulting in the movement of the contour intersection. Marginal contour crossings of the dashed lines are additionally observed at $R/L_n \sim 4$ and 6, however these are ignored in this analysis due to their disagreement with the predicted crossing from figure 9(b). These marginal crossings are likely the result of the grid resolution which was chosen to balance accuracy and speed of the calculation.

Now that the effect of powder injection on the particle flux and heat flux contours has been demonstrated, the next step was to evaluate which parameters were most responsible for the higher R/L_n and higher R/L_{T_i} contour crossing during the B drop. Six parameters known to impact plasma stability were evaluated: the effective ion charge Z_{eff}, the normalized electron collisionality ν_e^*, the electron/ion temperature ratio T_e/T_i, the normalized pressure gradient α, the safety factor q, and the magnetic shear s. Nominal values of these parameters from before ($t = 6.4$ s) and during ($t = 7.2$ s) the B drop are shown in table 2. These values (aside from Z_{eff} at $t = 7.2$ s) were taken from the predictive HFPS simulations described earlier and were therefore evolved self-consistently. Because Z_{eff} could not be measured during the LHCD phase, it was manually adjusted from 1.73 to 3.0 in the gyrokinetic modeling to approximate the B drop. This value assumed that all the B had been ionized and provided an upper bound on the impact of Z_{eff}.

Table 2. Values of Z_{eff}, ν_e^*, T_e/T_i, α, q, s from the HFPS simulations before (t = 6.4 s) and during ($t = 7.2$ s) the B drop and at $\rho = 0.5$ and $\rho = 0.65$. $*Z_{\mathrm{eff}}$ was held constant in the HFPS simulation, but manually set to 3.0 at $t = 7.2$ s in the QuaLiKiz simulations to approximate the B powder drop.

	$\rho = 0.5$		$\rho = 0.65$	
Time	$t = 6.4$ s	$t = 7.2$ s	$t = 6.4$ s	$t = 7.2$ s
Z_{eff} (Ohmic)	1.73	3.0*	1.73	3.0*
ν_e^*	0.65	1.33	1.13	2.15
T_e/T_{i}	1.88	1.48	1.54	1.33
α	0.15	0.21	0.19	0.26
q	1.71	1.73	2.17	2.18
s	0.91	0.95	1.31	1.32

To isolate the parameter(s) responsible for the change in the contour crossing, QuaLiKiz simulations of the pre-drop phase ($t = 6.4$ s) were run with modified inputs. We note that this disrupts the self-consistency from the HPFS simulations, however this method provides useful insight into de-correlating the impact of each individual stability parameter. The goal of this analysis was to reproduce the enhanced R/L_n and R/L_{T_i} of the contour crossing in figure 9 and thus the predicted R/L_{T_i} and R/L_n observed in the QuaLiKiz simulation at $t = 7.2$ s. For example, to isolate the impact of collisionality on the contour crossing at $\rho = 0.5$, QuaLiKiz would be set up to run the $t = 6.4$ s case, however instead of using the original value of $\nu_e^* = 0.65$, the drop phase ($t = 7.2$ s) value of $\nu_e^* = 1.33$ would be used instead. This was done for all six parameters of interest using the ranges shown in table 2. The following sections will describe the impact of various parameters on the Γ_e and Q_e/Q_{i} contour crossing at $\rho = 0.5$ and $\rho = 0.65$.

4.2. Impact of ν_e^*, Z_{eff}, and T_e/T_i at $\rho = 0.5$

At mid radius, the three parameters that had the largest impact in these simulations were ν_e^*, Z_{eff}, and T_e/T_{i}. This is somewhat expected as these parameters had the largest differences between their pre-drop phase and drop phase values. While the increase in Z_{eff} was by design, the increase in collisionality can be attributed to the strong rise in density ($\nu_e^* \propto n_e$) due to the ionization of the B powder. Increased ion temperatures from the improved confinement led to a decrease in the T_e/T_{i} ratio which may have led to further reductions in turbulence. Modification of α, q, and s had little impact on the contour crossing for the ranges from table 2 and were unable to

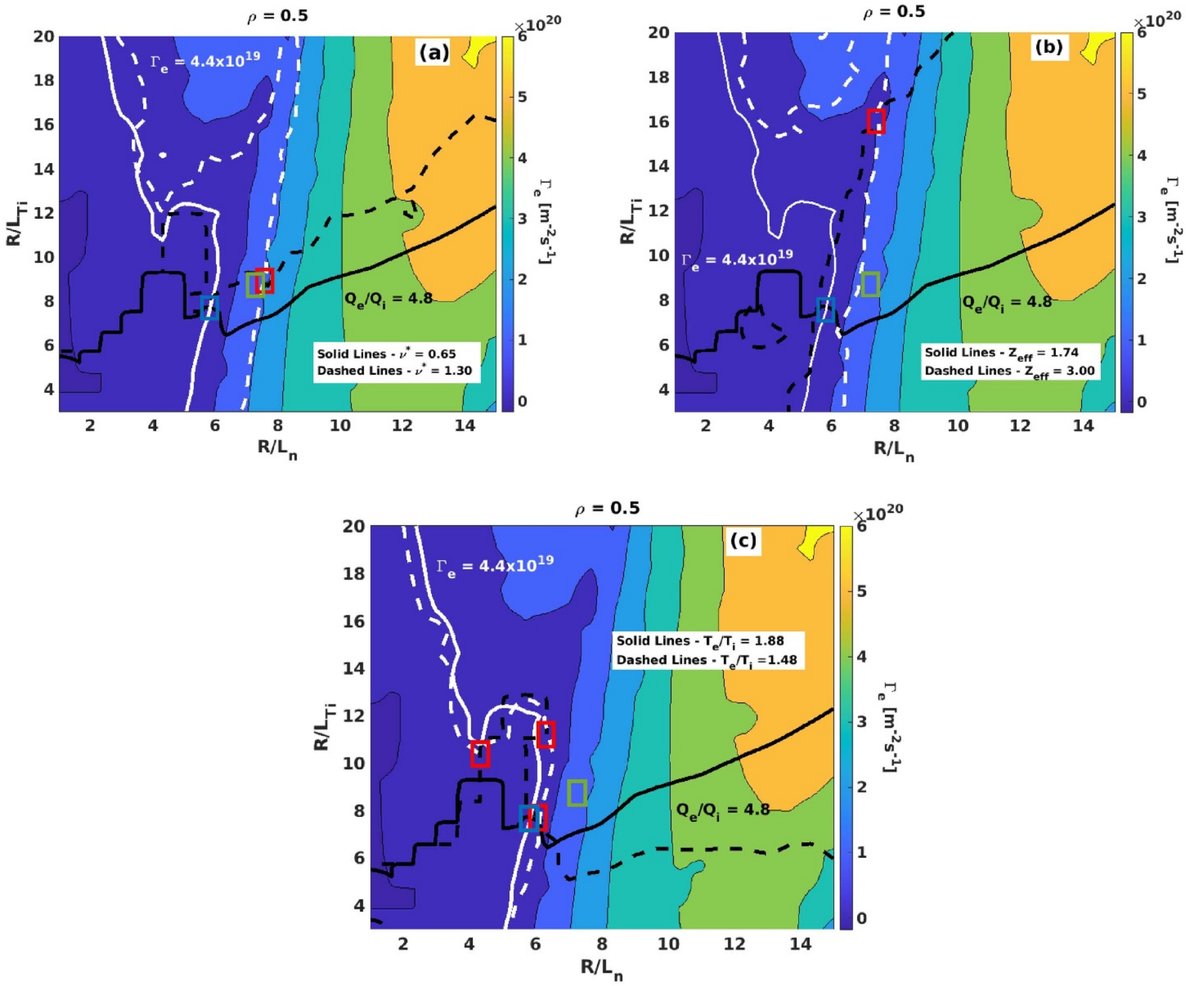

Figure 13. Γ_e and Q_e/Q_i contours for simulations with modified (a) ν_e^*, (b) Z_eff, and (c) T_e/T_i at $\rho = 0.5$. Solid lines correspond to simulations with the default parameters from $t = 6.4$ s. Dashed lines correspond to simulations with the modified parameters. The blue and green boxes represent contour crossings from the original simulations at $t = 6.4$ s and $t = 7.2$ s. The red boxes represent contour crossings from modified $t = 6.4$ s simulations.

individually reproduce the impact of powder injection. These contours plots are therefore not shown for brevity.

The impact of collisionality on the Γ_e and Q_e/Q_i contours is shown in figure 13(a). Here, the blue box represents the contour crossing of the original $t = 6.4$ s simulation, the red box represents the contour crossing of the modified $t = 6.4$ s simulation, and the green box shows the original $t = 7.2$ s simulation for reference. Collisionality has long been known to be a mechanism for turbulence suppression, particularly transport driven by TEMs. Increasing collisionality can result in the collisional de-trapping of electrons in banana orbits which leads to smaller contributions from TEM-driven turbulence. In regimes of very high collisionality, the TEM-driven turbulence can be completely suppressed [38]. Similar to figure 12, the contour crossing (red box) was moved towards higher R/L_n and higher R/L_{T_i} in quantitative agreement with the HFPS results. This suggests that the increase in collisionality is a key parameter explaining the increase in density peaking and in confinement.

Increased Z_eff is additionally known to suppress turbulence through the dilution of the main ions which reduces the drive for ITG modes [38]. In contrast to the collisionality, the impact of Z_eff on the contour crossing (figure 13(b)), has a much more overstated effect. Here, the contour crossing is moved to significantly higher R/L_{T_i} than predicted in the $t = 7.2$ s simulation (green box). This disagreement likely stems from the uncertainty in the chosen Z_eff and the predicted T_i. It is possible that not all the B powder was ionized or that the Z_eff profile was not flat and reduced values are obtained at the mid-plane in comparison to the edge. This would result in a more modest increase in Z_eff at mid-radius and possibly a reduced increase in the R/L_{T_i} at the contour crossing. When the simulation was repeated with $Z_\mathrm{eff} = 2.5$ instead of 3, the results showed a more reasonable estimation of $R/L_{T_\mathrm{i}} \sim 11$. Therefore, Z_eff still remains a possible candidate behind the improved confinement at $\rho = 0.5$.

An important takeaway, however, is the potential impact of Z_eff for future powder injection experiments. If Z_eff does result in this large increase in R/L_{T_i}, it may be attractive to increase Z_eff to higher values to possibly obtain even larger improvements in confinement. This is somewhat reminiscent of the RI-mode critical Z_eff threshold mentioned previously, where

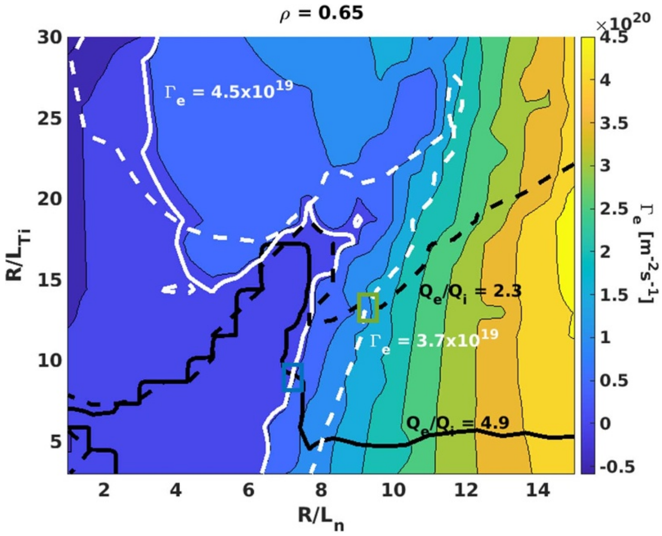

Figure 14. Contours of electron particle flux and electron/ion heat flux from QuaLiKiz at $t = 6.4$ s and $t = 7.2$ s and $\rho = 0.65$. The solid lines correspond to simulations before the B drop ($t = 6.4$ s) and dashed lines correspond to simulations after the B drop ($t = 7.2$ s). The colored contours in the background only correspond to $t = 6.4$ s.

density profile bifurcation could not be reproduced in some devices at low values of Z_{eff}.

Notably, both ν^* and Z_{eff} had large impacts on the particle flux contours (solid white lines and dashed white lines). In both cases, the particle flux contour was pushed to larger values of R/L_n and R/L_{T_i}, creating a valley towards higher ion temperatures and increased density peaking. Taking advantage of this operating space may additionally lead to larger improvements in confinement in the future.

Lastly, the impact of T_e/T_i on the resultant particle and heat fluxes is shown in figure 13(c). In this case, there were multiple contour crossings making the interpretation not straightforward. Lower T_e/T_i is expected to stabilize further ITG-driven turbulence at low density gradient lengths [38]. This can be seen in the heat flux ratio contours (solid and dashed black lines) in figure 13(c), where a valley towards larger R/L_{T_i} opens as T_e/T_i is reduced. Figure 10 shows that the injection of B powder is predicted to increase R/L_n, thanks to higher ν_e^* and Z_{eff}. The reduction of T_e/T_i only leads to an increased R/L_{T_i}. Therefore, T_e/T_i is not believed to have been a dominant mechanism in the triggering of improvements in confinement at mid-radius, but likely it helps to lock in the improved R/L_{T_i} value over time.

4.3. Impact of ν_e^*, Z_{eff}, and T_e/T_i at $\rho = 0.65$

Gyrokinetic analysis was additionally performed at $\rho = 0.65$ to assess the impact of powder injection on particle and heat fluxes closer to the injection location. Similar to $\rho = 0.5$, ν_e^*, Z_{eff}, and T_e/T_i had the largest changes from the pre-drop to the drop-phase (see table 2) and are therefore the only parameters shown here. The change in the contour crossing from $t = 6.4$ s to $t = 7.2$ s at $\rho = 0.65$ is shown in figure 14. The B drop moved the contour crossing to higher R/L_{T_i} and R/L_n, mimicking the change in crossing from $\rho = 0.5$ albeit at higher values.

The same gyrokinetic analysis performed at $\rho = 0.5$ was extended to $\rho = 0.65$. The change in contour crossing based upon the modified ν_e^*, Z_{eff}, and T_e/T_i are shown in figures 15(a)–(c), respectively. Unlike in figure 13(a), modifying the pre-drop collisionality to the drop phase ($t = 7.2$ s) value did not result in good reproduction of the drop phase contour crossing. Instead, increasing the collisionality only led to a substantial increase in the density gradient length. In the case where the pre-drop phase Z_{eff} was modified, the contour crossing showed relatively good agreement with the drop phase contours. While this result suggests that Z_{eff} may play the dominant role at $\rho = 0.65$, the predicted contour crossing at $t = 7.2$ s (green box) was calculated without modifications to Z_{eff}. Therefore, HFPS modeling suggests that other mechanisms should be able to reproduce this contour crossing. While increased collisionality alone could not reproduce the $t = 7.2$ s crossing, it is possible that the combination of increased collisionality and decreased T_e/T_i may lead to a comparable crossing. As seen in figure 15(c), modification of T_e/T_i produced a slight shift to higher R/L_{T_i}. The combination of this increase in R/L_{T_i} from T_e/T_i with the increase in R/L_n from ν_e^* produces a contour crossing close to the HFPS simulation at $t = 7.2$ s.

It is not immediately clear why the mechanism behind the increased gradient lengths differs based on radial location. At mid-radius, collisionality may dominate due to the increased density peaking and large change in ν_e^*. Additionally, the turbulence composition at each radial location may play a significant role. The trapped particle fraction is expected to be larger closer to the plasma edge, therefore collisionality may need to be increased further to sufficiently suppress TEM-drive turbulence. Lastly, the Z_{eff} radial distribution should be considered if Z_{eff} is determined to be a significant factor. At higher normalized radius, a large estimate of Z_{eff} may be more consistent with the experimental data, while closer to the core, Z_{eff} may be expected to be lower. Future work will investigate these radial dependencies further with more extensive

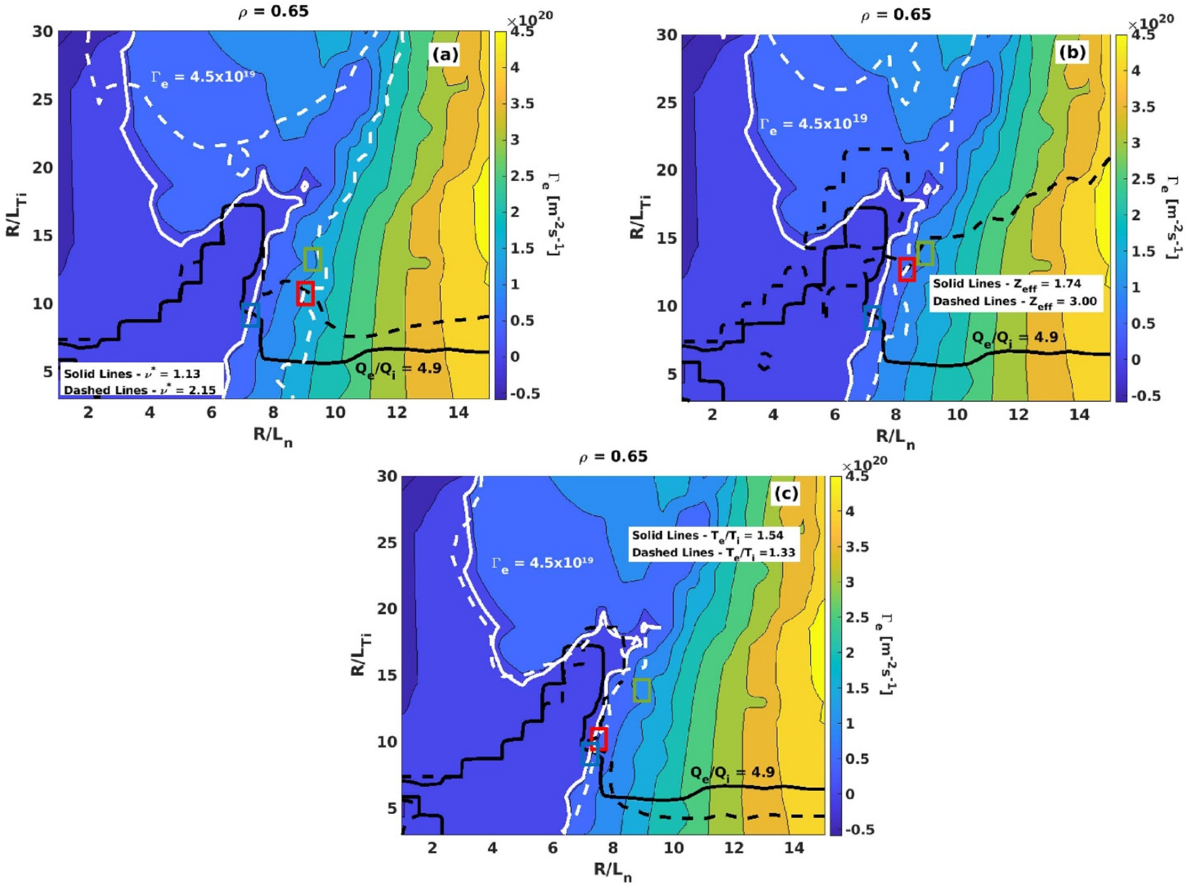

Figure 15. Γ_e and Q_e/Q_i contours for simulations with modified (a) ν_e^*, (b) Z_eff, and (c) T_e/T_i at $\rho = 0.65$. Solid lines correspond to simulations with the default parameters from $t = 6.4$ s. Dashed lines correspond to simulations with the modified parameters.

diagnostic suites that should provide better constraints for simulations.

5. Conclusion

B powder injection experiments on WEST have observed noticeable improvements in confinement without triggering an L-H transition. These results were reminiscent of RI-modes and may be attractive for future fusion devices due to the concurrent wall conditioning and edge radiation offered by powder injection. In order to exploit these results in future experiments, an interpretative modeling framework was developed to investigate the mechanisms behind the improvements in confinement.

The input to the HFPS was based on a combination of fits of measured quantities (T_e, n_e) and inferred quantities from integrating modeling such as W_MHD from the NICE reconstruction code and $T_\mathrm{i}, Z_\mathrm{eff}$ from METIS. Using the HFPS, in combination with predictive turbulent heat and particle fluxes from QuaLiKiz, the T_e and T_i profiles were predicted dynamically from $t = 4 - 7.4$ s and from $\rho = 0 - 0.8$. The predicted profiles showed good consistency with the experimental measurements from interferometry and ECE across the entire time window. The total energy content predicted was within 30% of the MHD equilibrium value and the increment of energy content as a result of the B drop was captured (+70 kJ in the MHD equilibrium reconstruction and +60 kJ in the predictive modeling). The flux-driven integrated modeling showed higher R/L_{T_i} and R/L_n at both $\rho = 0.5$ and $\rho = 0.65$ as a result of the B drop. The main differences between the pre-drop and drop phase plasma parameters were an enhanced collisionality, a reduced T_e/T_i, and an increased Z_{eff}.

To understand which of these parameters was the most responsible for the increase in ion temperature and particle confinement during the B drop, a stability analysis using gyrokinetic modeling was performed. The code QuaLiKiz was used in stand-alone fashion for this exercise at both radii. The identified parameters were modified individually to attempt to decorrelate their respective impacts.

In these simulations, collisionality was found to most accurately reproduce the predicted change in normalized gradient lengths at $\rho = 0.5$. There may be possible contributions from increased Z_eff (i.e. increased fuel dilution), however a more reasonable estimate than $Z_\mathrm{eff} = 3$ needs to be made (future experiments will determine if this is justified). At $\rho = 0.65$, modification of Z_eff led to good reproduction of the predicted increased in R/L_{T_i} and R/L_n, however the assumption of constant Z_eff in the HFPS modeling suggested other mechanisms could additionally produce the predicted result.

While collisionality alone was unable to match the predicted enhancement, the combination of effects from collisionality and T_e/T_i were consistent with enhanced R/L_{T_i} and R/L_n. We note, however, that the T_e/T_i contour crossings were more marginal than those at $\rho = 0.5$ and could be impacted by slight variations in the contour values.

In summary, higher collisionality, lower T_e/T_i, and higher Z_eff were determined to be the most likely candidates for the improved confinement during B powder injection in WEST L-mode discharges. The change in these parameters resulted in core density peaking observed in both the interferometry measurements and through the increasing density gradient length in the gyrokinetic analysis. Enhancing Z_eff to improve core performance can lead to fuel dilution in a burning plasma which might be counter productive if the improvement of the ion energy is not counter balancing the fuel dilution.

Future experiments should seek to find the optimal values of ν_e^*, T_e/T_i, and Z_eff by modifying the powder drop rate and amount of powder injected. This is planned for the WEST C8 campaign which will drop boron and boron-nitride at higher drop rates into higher-power plasmas in the hopes of obtaining even larger improvements in confinement. The combination of the modeling framework developed in this paper and an enhanced diagnostic set (expected in the upcoming campaign), should enable further clarification of the mechanisms behind the increased confinement and at more radial locations, preferably at the core and closer to the injection site. The results of these simulations and experiments will provide a basis from which to exploit powder injection as a tool for not only wall conditioning, but improved confinement as well.

Data availability statement

The data that support the findings of this study are openly available at the following URL/DOI: https://doi.org/10.34770/hr5y-c816.

Acknowledgments

The authors would like to thank the WEST team and the ORNL PMI group for their support of the IPD experiments (particularly F-P Pellisier, J Morales, M De Combarieu, J F Artaud, D Vézinet, and C Gil).

This manuscript is based upon work supported by the U.S. Department of Energy, Office of Science, Office of Fusion Energy Sciences, and has been authored by Princeton University under Contract Number DE-AC02-09CH11466 with the U.S. Department of Energy. The publisher, by accepting the article for publication acknowledges, that the United States Government retains a non-exclusive, paid-up, irrevocable, world-wide license to publish or reproduce the published form of this manuscript, or allow others to do so, for United States Government purposes.

Conflict of interest

The authors have no conflicts to disclose [39].

ORCID iDs

G Bodner https://orcid.org/0000-0003-2497-9172
C Bourdelle https://orcid.org/0000-0002-4096-8978
A Gallo https://orcid.org/0000-0002-7472-7830
K Afonin https://orcid.org/0000-0002-5479-2897
A Diallo https://orcid.org/0000-0002-0706-060X
R Lunsford https://orcid.org/0000-0003-3588-6801

References

[1] ITER Physics Expert Group on Divertor 1999 Chapter 4: power and particle control *Nucl. Fusion* **39** 2391
[2] Kuang A *et al* 2020 Divertor heat flux challenge and mitigation in SPARC *J. Plasma Phys.* **86** 865860505
[3] Rodriguez-Fernandez P *et al* 2022 Overview of the SPARC physics basis towards the exploration of burning-plasma regimes in high-field, compact tokamaks *Nucl. Fusion* **62** 042003
[4] Joffrin E *et al* 2014 First scenario development with the JET new ITER-like wall *Nucl. Fusion* **54** 013011
[5] Matthews G F 1995 Plasma detachment from divertor targets and limiters *J. Nucl. Instrum.* **220–222** 104–16
[6] Lazarus E A *et al* 1984 Confinement improvement in beam heated ISX-B discharges with low-z impurity injection *J. Nucl. Mater.* **121** 61–68
[7] McKee G, Burrell K, Fonck R, Jackson G, Murakami M, Staebler G, Thomas D and West P 2000 Impurity-induced suppression of core turbulence and transport in the DIII-D tokamak *Phys. Rev. Lett.* **84** 1922
[8] Unterberg B, Samm U, Tokar M Z, Messiaen A M, Ongena J and Jaspers R 2005 The radiative improved mode in TEXTOR: power exhaust and improved confinement at high density *Fusion Sci. Technol.* **47** 187
[9] Nagy A, Bortolon A, Mauzey D M, Wolfe E, Gilson E P, Lunsford R, Maingi R, Mansfield D K, Nazikian R and Roquemore A L 2018 A multi-species powder dropper for magnetic fusion applications *Rev. Sci. Instrum.* **89** 10K121
[10] Bortolon A *et al* 2019 Real-time wall conditioning by controlled injection of boron and boron nitride powder in full tungsten wall ASDEX Upgrade *Nucl. Mater. Energy* **19** 384–9
[11] Lunsford R *et al* 2019 Active conditioning of ASDEX Upgrade tungsten plasma-facing components and discharge enhancement through boron and boron nitride particulate injection *Nucl. Fusion* **59** 126034
[12] Xu W *et al* 2021 Comparison of active impurity control between lithium and boron powder real-time injection in EAST, 2021 *Phys. Scr.* **96** 124034
[13] Effenberg F *et al* 2022 Mitigation of plasma-wall interactions with low-Z powders in DIII-D high confinement plasmas *Nucl. Fusion* **62** 106015
[14] Gilson E P *et al* 2021 Wall conditioning and ELM mitigation with boron nitride powder injection in KSTAR *Nucl. Mater. Energy* **28** 101043
[15] Lunsford R *et al* 2021 Characterization of injection and confinement improvement through impurity induced profile modifications on the Wendelstein 7-X stellarator *Phys. Plasmas* **28** 082506
[16] Lunsford R *et al* 2022 Real-time wall conditioning and recycling modification utilizing boron and boron nitride powder injections into the Large Helical Device *Nucl. Fusion* **62** 086021
[17] Bodner G *et al* 2022 Initial results from boron powder injection experiments in WEST lower single null L-mode plasmas *Nucl. Fusion* **62** 086020

[18] Bucalossi J *et al* 2014 The WEST project: testing ITER divertor high heat flux component technology in a steady state tokamak environment *Fusion Eng. Des.* **89** 907–91

[19] Bourdelle C *et al* 2015 WEST physics basis *Nucl. Fusion* **55** 063017

[20] Bucalossi J *et al* 2022 Operating a full tungsten actively cooled tokamak: overview of WEST first phase of operation *Nucl. Fusion* **62** 042007

[21] Hu J S *et al* 2015 New steady-state quiescent high-confinement plasma in an experimental advanced superconducting tokamak *Phys. Rev. Lett.* **114** 055001

[22] Maingi R *et al* 2018 ELM elimination with Li powder injection in EAST discharges using the tungsten upper divertor *Nucl. Fusion* **58** 024003

[23] Sun Z *et al* 2021 Suppression of edge localized modes with real-time boron injection using the tungsten divertor in EAST *Nucl. Fusion* **61** 014002

[24] Maingi R *et al* 2020 ELM suppression by boron powder injection and comparison with lithium powder injection on EAST *J. Fusion Energy* **39** 429–35

[25] Osborne T H *et al* 2015 Enhanced H-mode pedestals with lithium injection in DIII-D *Nucl. Fusion* **55** 063018

[26] Mansfield D K, Roquemore A L, Schneider H, Timberlake J, Kugel H and Bell M G (the NSXT Research Team) 2010 A simple apparatus for the injection of lithium aerosol into the scrape-off layer of fusion research devices *Fusion Eng. Des.* **85** 890–5

[27] Nespoli F *et al* 2022 Observation of a reduced-turbulence regime with boron powder injection in a stellarator *Nat. Phys.* **18** 350–6

[28] Vermare L *et al* 2022 Formation of the radial electric field profile in the WEST tokamak *Nucl. Fusion* **62** 026002

[29] Afonin K *et al* 2023 Interpretive modelling of boron transport in the boundary plasma of WEST experiments with the impurity powder dropper *Nucl. Fusion* **63** 126057

[30] Yang X *et al* 2020 Core tungsten transport in WEST long pulse L-mode plasmas *Nucl. Fusion* **60** 086012

[31] Artaud J F *et al* 2018 Metis: a fast integrated tokamak modelling tool for scenario design *Nucl. Fusion* **58** 105001

[32] Cenacchi G and Taroni A 1988 JETTO: a free boundary plasma transport code *ENEA RT/TIP Report* vol 88 p 5 (available at: https://inis.iaea.org/search/search.aspx?orig_q=RN:19097143)

[33] Bourdelle C, Citrin J, Baiocchi B, Casati A, Cottier P, Garbet X and Imbeaux F (JET Contributors) 2015 Core turbulent transport in tokamak plasmas: bridging theory and experiment with QuaLiKiz *Plasma Phys. Control. Fusion* **58** 014036

[34] Faugeras B and Orsitto F (JET Contributors) 2018 Equilibrium reconstruction at JET using Stokes model for polarimetry *Nucl. Fusion* **58** 10

[35] Romanelli M *et al* 2014 JINTRAC: a system of codes for integrated simulation of tokamak scenarios *Plasma Fusion Res.* **9** 3403023

[36] Asp E, Weiland J, Garbet X, Mantica P, Parail V and Suttrop W (the EFDA-JET Contributors) 2005 JETTO simulations of *Te/Ti* effects on plasma confinement *Plasma Phys. Control. Fusion* **47** 505

[37] Stephens C D, Garbet X, Citrin J, Bourdelle C, van de Plassche K L and Jenko F 2021 Quasilinear gyrokinetic theory: A derivation of QuaLiKiz *J. Plasma Phys.* **87** 905870409

[38] Bourdelle C 2015 Turbulent transport in tokamak plasmas: bridging theory and experiment *Doctoral Dissertation* Aix Marseille Université

[39] Bodner G *et al* 2024 Stability analysis of WEST L-mode discharges with improved confinement from boron powder injection [Dataset] (Princeton Plasma Physics Laboratory, Princeton University) (https://doi.org/10.34770/hr5y-c816)